

# Precise Real-Time Relative Orbit Determination for Large-Baseline Formations Using GNSS

Vincent Giraldo, *Space Rendezvous Laboratory, Stanford University, Stanford, CA, United States*  
Simone D'Amico, *Space Rendezvous Laboratory, Stanford University, Stanford, CA, United States*

## BIOGRAPHIES

**Vincent Giraldo** is a doctoral candidate in the Space Rendezvous Laboratory. He graduated from Bucknell University with a B.S. in Mechanical Engineering, as well as receiving his M.S. from Stanford University in Aeronautics and Astronautics. His current research focuses on using GNSS technology for precise relative navigation of distributed space systems.

**Simone D'Amico** is an Associate Professor of Aeronautics and Astronautics at Stanford University, a W. M. Keck Faculty Scholar in the School of Engineering, Founder and Director of the Space Rendezvous Laboratory, and Satellite Advisor of the Student Space Initiative, Stanford's largest undergraduate organization. He received his B.S. and M.S. from Politecnico di Milano and his Ph.D. from Delft University of Technology.

## ABSTRACT

This paper presents a real-time GNSS-based navigation architecture for distributed space systems, which performs precise relative orbit determination at separations of hundreds of kilometers. Through differential carrier-phase GNSS and on-board integer ambiguity resolution, a hybrid Kalman filter combines the extended Kalman filter time update with the unscented Kalman filter measurement update to exploit nonlinearities in separation-dependent errors while minimizing computational load. Differential ionospheric path delays on multiple frequencies are modeled through the Klobuchar model with an estimated correction term to account for unmodeled effects. This method allows the filter to use low-noise single-difference carrier-phase measurements at large separations to provide relative navigation solutions with centimeter-level error.

## I. INTRODUCTION

This work presents an on-board navigation approach for Distributed Space Systems (DSS) that extends beyond typical Low Earth Orbit (LEO) scenarios to large separations through the use of Global Navigation Satellite Systems (GNSS). DSS make use of two or more interacting spacecraft to accomplish scientific or commercial objectives otherwise impossible or very difficult to achieve through a single platform. DSS promise breakthrough applications in astrophysics and astronomy [1], on-orbit servicing and assembly [2], and planetary science such as synthetic aperture radar interferometry [3], to name a few. Several advanced DSS mission concepts require precise on-board knowledge of the absolute and relative orbits of the participating satellites at diverse separations to be successful [4, 5, 6]. This presents difficulties to the on-board navigation system, requiring unprecedented levels of precision. The work presented in this paper addresses new strategies that provide DSS with the necessary precision to meet mission requirements while operating at large separations.

One such mission is the Miniaturized Distributed Occulter/Telescope (mDOT, Pre-Phase A) [4]. With the goal of directly imaging extrasolar dust disks and large exoplanets, mDOT consists of two spacecraft in a sun-synchronous low Earth orbit with a nominal separation of 500km. To maintain pointing with an inertial target, the formation requires relative positioning knowledge of 2cm (3D, RMS) in the presence of maneuvers that both preserve alignment and reconfigure the formation [7]. Another advanced mission concept is the Virtual Super-resolution Optics with Reconfigurable Swarms (VISORS, 2024), a formation of two CubeSats that will study the solar corona to test theories of coronal heating [5, 8]. This mission requires spacecraft separations as low as 20m with a relative position control window of  $\pm 15$ mm during the science phase. To meet these requirements, highly frequent maneuvers must be executed while maintaining navigation precision. For both mDOT and VISORS, the baseline navigation system foreseen utilizes differential GNSS (dGNSS) during operation.

GNSS-based navigation is an enabling technology for many satellite missions. Absolute positioning accuracies of less than 1m have been reported for a single spacecraft in real time, with relative positioning accuracies much lower through the use of dGNSS [9]. By exploiting differential measurements between receivers, common errors can be cancelled out. High-precision real-time navigation has been demonstrated on missions such as PRISMA (2010, Swedish Space Corporation) [10, 11, 12, 13]. Consisting of two spacecraft, the on-board Extended Kalman Filter (EKF) showed precise relative navigation capabilities of less than 10cm (3D, RMS) of relative positioning error in real time throughout most mission scenarios. Similar results have been obtained by CanX-4/5 (2014, University of Toronto) using smaller nanosatellites [14, 15, 16].

Navigation accuracies have been further improved upon by performing the additional step of fixing the carrier-phase ambiguities. However, Integer Ambiguity Resolution (IAR) has never been achieved or attempted on board due to high computational overhead and no guarantee of correctly solving for the ambiguities. Through post-processing with precise GPS orbit products, the Gravity Recovery and Climate Experiment (GRACE, 2002) mission demonstrated 1mm (1D range-only,  $1\sigma$ ) relative positioning accuracy at a separation of 200km when compared with the high-precision on-board K/Ka-band ranging system [17, 18, 19]. More recently, advances have been made to flight avionics that enable the capability of performing IAR on board. The Distributed Multi-GNSS Timing and Localization system (DiGiTaL) is a navigation payload for nanosatellites that achieves centimeter-level positioning accuracy and nanosecond-level time synchronization throughout arbitrarily sized swarms [20]. A reduced-dynamics estimation architecture on board each individual nanosatellite processes low-noise measurements from multiple GNSS constellations and frequencies to reconstruct the full formation state with high accuracy. DiGiTaL demonstrated successful IAR to provide less than 1cm (1D, RMS) of relative positioning accuracy in real time for a swarm of four spacecraft over short baselines using full CubeSat avionics in the loop [21]. The technology will be demonstrated in flight for the first time on the Demonstration With nanosatellites of Autonomous Rendezvous and Formation-flying (DWARF) mission, a binary formation under development by KACST (Saudi Arabia) and Stanford University and set for launch in 2022 [22]. DiGiTaL is also the primary navigation system selected for mDOT and VISORS and is a mission-enabling technology [4, 5].

While previous work has shown precision navigation for DSS, there have been no examples capable of meeting the requirements of advanced missions. GRACE was able to demonstrate the required navigation accuracy for large separations, but this was done in post-processing where timeliness is not considered. DiGiTaL is capable of demonstrating real-time precise navigation using IAR, but has only been shown for small separations. For missions like mDOT to be successful, the shortcomings of the previous GNSS-based navigation systems must be addressed. In particular, this work highlights extensions to DiGiTaL that enable mDOT and other advanced mission concepts.

The capabilities of DiGiTaL have only been shown for spacecraft separations of less than 10km. For larger separations, common errors between receivers, such as ionospheric path delays and broadcast ephemeris errors of the GNSS satellites, are no longer mitigated through differential measurements. Therefore, other methods must be used to handle these increasing errors. A common method for eliminating ionospheric path delays is through the use of dual-frequency signals, where the delay can be eliminated to first-order [17]. However, this combination inherently increases the measurement noise, which limits the achievable precision for relative navigation and also removes the integer nature of the carrier-phase ambiguity. This work employs a new strategy for handling ionospheric path delay between the spacecraft by combining the well-known Klobuchar model [23] with an estimated correction term. By augmenting the filter state with the differential correction and adopting the measurement update from the Unscented Kalman Filter (UKF), a hybrid Extended/Unscented Kalman Filter (E/UKF) can better handle measurement nonlinearities at large baselines without unnecessarily increasing the computational load during orbit propagation. The estimated ionospheric delay is utilized to form the lower-noise single-frequency measurements that maintain the integer values of the ambiguities. With this method, DiGiTaL is capable of maintaining high levels of precision while expanding the baseline between spacecraft to hundreds of kilometers.

These extensions to DiGiTaL underwent extensive software-in-the-loop testing to ensure that the mission requirements of mDOT were met. Using Stanford University's GNSS and Radiofrequency Testbed for Autonomous Navigation of DSS (GRAND) [24], the new algorithms show that DiGiTaL's centimeter-level precision can be extended to separations of 500km without compromising timeliness. This paper demonstrates that the DiGiTaL navigation payload can meet mission requirements that enable future miniaturized DSS at large separations.

Following this introduction, an overview of the DiGiTaL system is presented with details on the orbit determination method. The next section provides the methodology for extending the inter-spacecraft separation through augmentations to the nominal DiGiTaL algorithms. Finally, a test case is examined to demonstrate DiGiTaL's capability to perform precision navigation at large baselines.

## II. DISTRIBUTED MULTI-GNSS TIMING AND LOCALIZATION

The DiGiTaL system is a plug-and-play navigation payload for nanosatellites that achieves centimeter-level relative positioning accuracy and nanosecond-level time synchronization throughout arbitrarily sized swarms to meet the strict requirements of advanced mission concepts [21]. Consisting of commercial-off-the-shelf (COTS) hardware, DiGiTaL has a 0.5U CubeSat volume footprint, with a mass of 225g and a maximum power requirement of 3W. This includes a multi-GNSS antenna/receiver system, a chip-scale atomic clock (CSAC), an intersatellite-link (ISL), and a dedicated flight computer. Note that the power requirement does not include the ISL. DiGiTaL shares synchronous low-noise carrier-phase measurements between co-orbiting satellites to form error-cancelling combinations in a filter to estimate the absolute and relative orbits.

Figure 1 illustrates DiGiTaL's hardware architecture. Two Tallysman TW3972E Embedded Triple Band GNSS antennas [25] are placed in anti-parallel directions to collect GNSS signals across multiple constellations and frequencies with near omnidirectional coverage. An RF switch selects which antenna has the most favorable pointing direction (for example, zenith

pointing in LEO) and sends the signals to a NovAtel OEM 628 High-Performance GNSS receiver [26]. The receiver, capable of processing the various multi-GNSS signals, sends the raw measurements to the local flight computer for processing and to the remote spacecraft via the ISL.

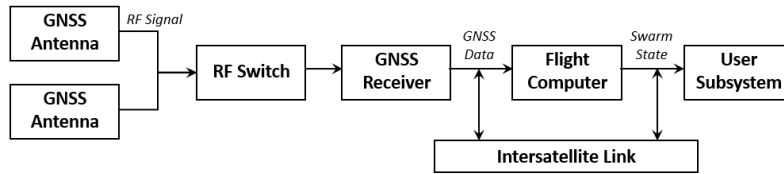


Figure 1: Hardware architecture of the DiGiTaL payload [21]

To provide precise orbit estimates in a timely manner, DiGiTaL divides a large swarm into smaller subsets of directed partnerships, forming a connected graph. This means that a path can be traced from one satellite to any other satellite in the swarm. Within each partnership, local estimation is performed, where dGNSS with IAR provides centimeter-level relative positioning accuracy between spacecraft. All of the available local estimates are shared throughout the rest of the swarm, where the data is fused to create a full swarm estimate. This strategy leverages the precision of dGNSS while limiting the restrictive computational load.

At a high level, the DiGiTaL software is divided into four modules. Figure 2 shows each module in yellow, along with associated data flow. The system receives data from the on-board GNSS receiver, in addition to the attitude and orbit control system (AOCS) system. This information, along with telecommands, is processed by the DiGiTaL Data Interface (DDIF) module, where relevant data is formatted and forwarded to the proper module. In particular, measurements from the local and remote GNSS receivers are checked for validity and synchronicity, and the receivers’ navigation solutions are used to initialize the on-board filter. DiGiTaL Orbit Determination (DOD) hosts the local estimation process. A reduced-dynamics navigation filter uses dGNSS techniques in conjunction with IAR to estimate the absolute inertial orbits of each spacecraft within the local subset, subject to precise relative orbit constraints from low-noise differential carrier-phase measurements. In addition, the offsets of each receiver’s clock are estimated and used to measure the time synchronicity of the local subset. The DiGiTaL Swarm Determination (DSD) module then collects the local estimates from the DOD modules on every spacecraft through the ISL and fuses them to form an estimate of the orbits of each spacecraft, preserving the precision from DOD in a computationally efficient manner. Due to the complexity of both DOD and DSD, they are run at the relatively long sample times of 30 seconds. However, external subsystems of the spacecraft may require orbit data at a higher rate, which is provided by the DiGiTaL Orbit Prediction (DOP) module. Here, orbit polynomial coefficients calculated during the numerical integration of DOD are interpolated to determine navigation solutions at the desired rate.

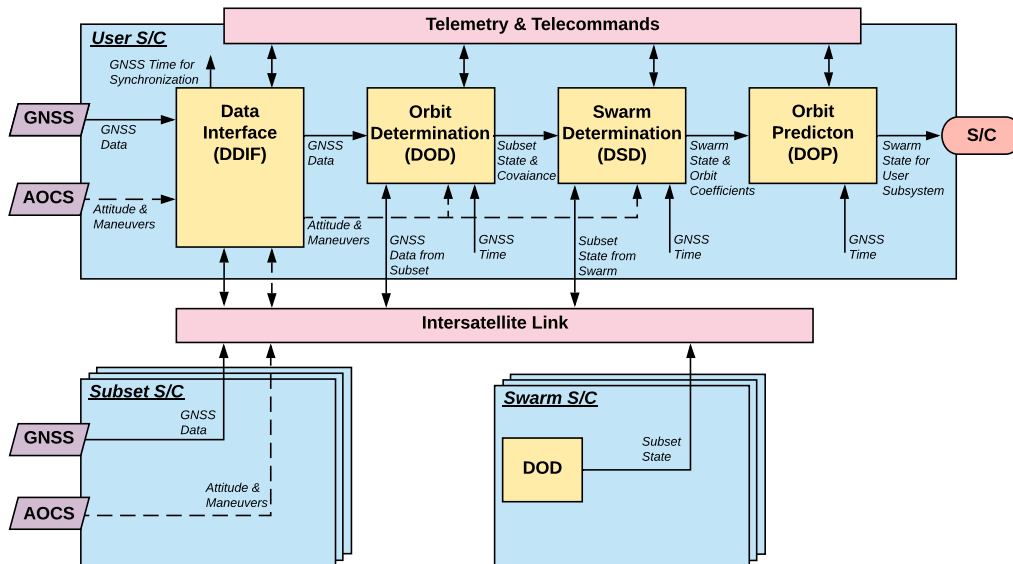


Figure 2: Software architecture of DiGiTaL [22]

## 1. DiGiTaL Orbit Determination

To contextualize the contributions of this paper, it is important to provide details of the original DOD algorithms. An EKF estimates the absolute inertial position,  $\mathbf{r}$ , and velocity,  $\mathbf{v}$  of each spacecraft in the local subset in the J2000 reference frame. This eliminates the need for an explicit relative state in the filter, along with removing reference frame transformations during the time update step. The orbits are propagated with DOD by numerically integrating the equations of motion with a reduced-dynamics model, including only a 20x20 spherical harmonic gravity field model [18]. To account for unmodelled dynamics in the filter, empirical accelerations,  $\mathbf{a}_e$ , are estimated as a first-order Gauss-Markov process. A fourth-order Runge-Kutta scheme numerically integrates the equations of motion with a Richardson step that provides polynomial coefficients. These orbit coefficients are used to interpolate the state and state transition matrix (STM) to the time of the next measurement during the time update and allows for a linear update of the covariance matrix [11].

When a maneuver is commanded, the filter propagates the state and covariance to the time of the maneuver. The commanded value of delta- $\mathbf{v}$  is added to the velocity components of the state, and process noise is added into the covariance matrix equal to 15% of the maneuver magnitude. This accounts for typical maneuver execution error through attitude uncertainty and mistimed maneuvers. In the filter, maneuvers are treated as impulses, resulting in an instantaneous change of velocity. Following the maneuver, the time update proceeds as normal, propagating to the time of either the next maneuver or measurement.

The full estimation state for DOD of a 2-satellite subset is given as

$$\mathbf{x} = [\mathbf{r}^c \quad \mathbf{v}^c \quad \mathbf{a}_e^c \quad \mathbf{cdt}^c \quad \mathbf{N}^c \quad \mathbf{r}^d \quad \mathbf{v}^d \quad \mathbf{a}_e^d \quad \mathbf{cdt}^d \quad \mathbf{N}^{dc}], \quad (1)$$

where superscripts  $c$  and  $d$  denote the local and remote spacecraft in the set, respectively. In addition to the position, velocity, and acceleration, the state also includes each GNSS receiver's clock bias from GNSS system time,  $\mathbf{cdt}$ , and the carrier-phase bias of each tracked signal,  $\mathbf{N}$ . The clock bias term, modelled as a random walk, is denoted as a vector since each GNSS constellation that is being considered operates on a separate time scale. Note that the state for each spacecraft is identical with the exception of the carrier-phase biases. In the local spacecraft state, these represent the undifferenced ambiguity, whereas in the remote spacecraft state, they are the single-differenced values between the two receivers, or  $N^{dc} = N^d - N^c$ . This design decision allows for the single-differenced ambiguities to be fixed during IAR, while retaining the degree of freedom on the undifferenced ambiguities. In a system with  $2m$  undifferenced ambiguities, the IAR process allows for the resolution of  $m$  single-differenced ambiguities. However, there is not enough information to solve for the  $2m$  undifferenced ambiguities without making assumptions for half of them. Therefore, the single-differenced ambiguities are fixed while the undifferenced ambiguities are left as floats. The float biases in the filter are treated as constant values with process noise during the propagation step.

Precision orbit determination in DiGiTaL is achieved through dGNSS using low-noise measurements in combination with IAR. The raw pseudorange and carrier-phase measurements [27] from the receiver are given as

$$\rho_{pr}(t) = \|\mathbf{r}(t) - \mathbf{r}(t - \tau)_{GNSS}\| + c(\delta t - \delta t_{GNSS}) + I + \epsilon_{pr} \quad (2)$$

$$\rho_{cp}(t) = \lambda\Phi = \|\mathbf{r}(t) - \mathbf{r}(t - \tau)_{GNSS}\| + c(\delta t - \delta t_{GNSS}) - I + \lambda N + \epsilon_{cp}. \quad (3)$$

Here,  $\mathbf{r}$  is the position of the phase-center of the receiving antenna, and  $\mathbf{r}_{GNSS}$  is the position of the phase-center of the transmitting antenna, offset by the signal travel time,  $\tau$ . While the state vector contains the inertial position, the GNSS systems operate in an Earth-fixed reference frame, and therefore a frame transformation is required to obtain the proper values. The clock offsets of both the receiver and GNSS service vehicle are given by  $\delta t$  and  $\delta t_{GNSS}$ , respectively, which are multiplied by the speed of light,  $c$ . The ionospheric path delay and carrier-phase ambiguity are given by  $I$  and  $N$ , respectively, with the latter being multiplied by the signal wavelength,  $\lambda$ . The noise on each measurement is given by  $\epsilon$ , which is on the order of 10cm for pseudorange and 1mm for carrier-phase.

DiGiTaL uses combinations of the raw observables defined by Eqs. (2) and (3) to form advantageous absolute and relative measurement types. A coarse absolute measurement is formed as the arithmetic mean of the code and phase, called the Group and Phase Ionospheric Correction (GRAPHIC) data type [28], given by

$$\rho_{gr}(t) = \frac{\rho_{pr} + \rho_{cp}}{2} = \|\mathbf{r}(t) - \mathbf{r}(t - \tau)_{GNSS}\| + c(\delta t - \delta t_{GNSS}) + \frac{\lambda}{2}N + \epsilon_{gr}, \quad (4)$$

which removes the ionospheric path delay and has noise on the order of  $\epsilon_{gr} \approx \epsilon_{pr}/2$ . A precise relative measurement is formed as the single-difference carrier-phase (SDCP) [17], given by

$$\rho_{sdcp} = \rho_{cp}^d - \rho_{cp}^c = \|\mathbf{r}(t) - \mathbf{r}(t - \tau)_{GNSS}\|^{dc} + c\delta t^{dc} - I^{dc} + \lambda N^{dc} + \epsilon_{sdcp}. \quad (5)$$

The SDCP measurements are formed as differences of carrier-phase measurements from two receivers, represented by  $c$  and  $d$ , tracking the same GNSS service vehicle. This creates a relative measurement between the receiving antennae's phase centers with millimeter-level noise. In this formulation,  $(\cdot)^{dc} = (\cdot)^d - (\cdot)^c$ . Note that the ionospheric delay is position dependent, meaning that the differential delay becomes negligible at short separations [29].

After the measurement update, the filter performs the additional step of IAR using the Modified Least-Squares Ambiguity Decorrelation Adjustment (mLAMBDA) method [30]. To fix the ambiguities, float-valued double-differenced carrier-phase (DDCP) ambiguities are formed by differencing two SDCP ambiguities from two GNSS satellites, or

$$N_{ddcp} = N_{sdcp}^k - N_{sdcp}^j, \quad (6)$$

where superscripts  $j$  and  $k$  represent different GNSS satellites. The DDCP ambiguities are then fixed to their integer values by mLAMBDA. By selecting a single reference GNSS satellite  $j$  to difference all others with, the SDCP ambiguities can be resolved and inserted back into the state. At this time, the ambiguities are treated as deterministic by zeroing out the corresponding rows and columns in the covariance matrix. As discussed above, the undifferenced ambiguities in the estimation state are left as stochastic quantities, treated as constants with added process noise.

To increase the robustness of the IAR process, a series of checks are performed including the Success Rate Test [31] and the Discrimination Test [32], as well as the novel Residual Test [21]. This final test checks the measurement residuals before and after the ambiguities are fixed to ensure that IAR did not incorrectly set the ambiguities, which would be seen as a bias in the post-fit residual of the corresponding measurement.

Table 1 is presented to summarize the models used in DiGiTaL. Numerical values for these models are provided in the *Validation* section.

**Table 1:** Models used in the DiGiTaL navigation framework [21]

Parameter	Model
Reference frame transformation	EME2000 [33]
Force model	20x20 GGM01S gravity field [18]
Numerical integration	Fourth-order Runge-Kutta Richardson extrapolation [11]
Empirical accelerations	First-order Gauss-Markov [11]
Receiver clock bias	Random walk
Carrier-phase bias	Constant value

In a hardware-in-the-loop test on CubeSat avionics, DiGiTaL demonstrated less than 1cm of relative positioning accuracy and less than 10ns of time synchronization among a swarm of four spacecraft [21]. It is important to note that these results were obtained in a scenario with a maximum inter-spacecraft separation of 2km.

### III. LARGE-BASELINE ESTIMATION

The key advantage of dGNSS is the cancellation of common errors to remove biases and uncertainty in the measurements. To accomplish this, DiGiTaL uses SDCP measurements, which explicitly remove the clock offset of the GNSS service vehicle that is being tracked. In the specific case of short baselines, defined as separations less than 10km in LEO [11], errors from both ionospheric path delays and broadcast ephemerides are also cancelled out between receivers. The removal of these errors is critical to achieve the levels of precision that are seen by DiGiTaL and required by mDOT and VISORS.

To further demonstrate the capabilities of DiGiTaL and the novel contributions of this work, a test case is presented in detail in the *Validation* section of this paper. The scenario will be used to analyze the efficacy of a variety of implementations presented in this work. In this test, the original implementation of DiGiTaL presented above provides less than 1cm of positioning accuracy between the two spacecraft orbiting with a nominal separation of 2km.

When the baseline increases beyond 10km, the separation-dependent errors grow to be on the order of tens of centimeters. These errors are strictly in the measurements themselves, meaning that they cannot be accounted for by empirical accelerations and additional process noise during the time update. An improved measurement model is required. Without doing so, the accuracy of the estimation solution from the filter is subject to large unknown biases. Additionally, the uncertainty in the filter increases, causing a much larger search space for IAR. This means a longer time to find the correct integer solution, if at all. In the worst case, an incorrect solution is found and causes divergence of the filter.

The test case in the *Validation* section demonstrates the initial implementation of DiGiTaL when applied to a formation with inter-spacecraft separation of 500km. As a result of separation-dependent effects, the relative position estimate is biased in the tangential direction, and there is an increase in uncertainty. This leads to the filter's inability to fix the carrier-phase ambiguity and an overall degradation of performance.

## 1. Ionospheric Delay Estimation

To provide a better measurement model for DiGiTaL, the differential ionospheric path delay for each signal is accounted for by combining the Klobuchar model [23] with an estimated correction term to account for unmodelled effects. This is akin to the estimation process for tropospheric delays for terrestrial applications [24]. For the GRACE mission, the differential ionospheric path delay was estimated directly, allowing for baseline extensions up to 200km [17]. Unlike GRACE, where separate filters and estimation schemes were used for absolute and relative positioning in post-processing, DiGiTaL provides a single unifying filter to accomplish both in real time. This means that DiGiTaL does not benefit from precise knowledge of the GNSS satellite positions nor the precise absolute orbit of the user spacecraft. This results in higher levels of uncertainty and potentially incorrect values of the estimated ionospheric delay as a whole. The Klobuchar model on DiGiTaL acts as a baseline estimate to model general trends in the ionosphere, such as large biases, and then the correction term can estimate smaller variations in these trends.

The formulation of this approach is given as

$$I^{dc} = I_K^{dc} + \Delta I^{dc}, \quad (7)$$

where subscript  $K$  represents the Klobuchar model and  $\Delta I^{dc}$  is the differential correction. Note that the Klobuchar model is a function of the receiver position, the GNSS satellite position, and two sets of coefficients,  $\alpha$  and  $\beta$  [23]. The delay predicted by Klobuchar in meters is given by

$$I_K = \begin{cases} cM \left[ D + A \cos \left( 2\pi \frac{(t-50400)}{P} \right) \right], & \text{if } |P| < 1.57 \\ cMD, & \text{else} \end{cases} \quad (8)$$

where  $c$  is the speed of light and  $t$  is the local time of the ionospheric pierce point (IPP), assumed to be the location of the receiver for a LEO spacecraft. The daytime variation caused by sunlight is governed by

$$A = \begin{cases} \sum_{i=0}^3 \alpha_i \phi_m^i, & \text{if } A > 0 \\ 0, & \text{if } A \leq 0 \end{cases} \quad (9)$$

$$P = \begin{cases} \sum_{i=0}^3 \beta_i \phi_m^i, & \text{if } P > 72000 \\ 72000, & \text{if } P \leq 72000 \end{cases} \quad (10)$$

in units of seconds, where  $\phi_m$  is the geomagnetic latitude of the IPP. In addition to the polynomial terms, a constant delay is added to account for the delay at night when the receiver is not in sunlight. In seconds, this is given by

$$D = 5 \times 10^{-9}. \quad (11)$$

Finally, the zenith delay is multiplied by a mapping factor to account for the elevation of the GNSS spacecraft with respect to the receiver. This is given as

$$M = 1 + 16(0.53 - e)^3, \quad (12)$$

where  $e$  is the elevation measured in semi-circles. It should be noted that the Klobuchar model is known to correct for only 50-60% of the total ionospheric delay [23], and thus should not be solely relied upon for precision navigation. Interestingly, it was found that knowledge of the coefficients is not necessary when adding the correction term. By assuming each  $\alpha_i$  and  $\beta_i$  to be zero, the model simplifies to

$$I_K = cMD. \quad (13)$$

Effectively, DiGiTaL is using the constant nighttime delay from Klobuchar to account for bias and then estimates the variations caused by solar activity as a random-walk process. This also removes reliance on the imprecise model.

It is also important to note the relationship of the ionospheric delay across signal frequencies, namely

$$I_{f_j} = \frac{f_i^2}{f_j^2} I_{f_i}, \quad (14)$$

where  $i$  and  $j$  represent two signals such as GPS  $L_1$  and  $L_2$ . Because of this relationship, it is only necessary to estimate the delay on the primary frequency ( $L_1$  in DiGiTaL) and then relate that to all other frequencies. This both reduces the overall size of the estimation state and enforces the correlation between measurements on multiple frequencies.

Therefore, the differential correction,  $\Delta \mathbf{I}^{dc}$ , can be estimated on each primary frequency signal and added to the state, analogous to the single-difference carrier-phase bias, resulting in

$$\mathbf{x} = [\mathbf{r}^c \quad \mathbf{v}^c \quad \mathbf{a}_e^c \quad \text{cdt}^c \quad \mathbf{N}^c \quad \mathbf{r}^d \quad \mathbf{v}^d \quad \mathbf{a}_e^d \quad \text{cdt}^d \quad \mathbf{N}^{dc} \quad \Delta \mathbf{I}^{dc}]. \quad (15)$$

For ease of bookkeeping, the size of the ionospheric delay vector is equal to the total number of receiver channels. If a channel does not contain a signal on the primary frequency but rather a signal on a secondary frequency like  $L_2$ , it is treated as an empty channel, or identically zero.

In the *Validation* section, the augmentation of the measurement model is applied to the original system. To incorporate this change to the EKF, the Jacobian of the measurement with respect to the new state elements is required, namely

$$\frac{\partial \rho_{sdep}}{\partial \Delta I^{dc}} = \begin{cases} -1, & \text{if frequency} = L_1 \\ -\frac{f_{L_1}^2}{f_j^2}, & \text{if frequency} \neq L_1. \end{cases} \quad (16)$$

It should be noted that the Klobuchar model is also a nonlinear function of the receiver position via the elevation of the GNSS satellite, but this dependency was not taken into account in the measurement sensitivity matrix due to the complex linearization of this function. Results in the *Validation* section show that while the addition of ionospheric delay estimation reduces the bias in the tangential direction by more than 50%, there is now a large variation in the position error in the radial direction. This indicates that the new state parameter alone does not provide the necessary precision and further steps must be taken.

## 2. Unscented Kalman Filter

In addition to the estimation of the differential ionospheric path delay, an Unscented Kalman Filter (UKF) is utilized to better handle nonlinearities in the estimation process as compared to an EKF. The EKF truncates the Taylor-series expansion of the nonlinear system to first-order, whereas the UKF uses a sampling-based approach to approximate the mean and covariance of the filter by the Unscented Transform (UT). This type of filter has been beneficial for space-based applications such as angles-only navigation [34] and asteroid gravity recover [35], characterized by poor observability or lack of a-priori information, respectively.

The UKF algorithm, which has the same high-level structure for both the time and measurement updates, begins by taking the mean and covariance of the filter and deterministically sampling a set of "sigma points". For an  $n$ -dimensional state,  $2n + 1$  sigma points are sampled. The sigma points,  $\chi$ , are formed by

$$\chi = [\mu \quad \mu + \mathbf{A} \quad \mu - \mathbf{A}], \quad (17)$$

where  $\mu$  is the state mean. To compute  $\mathbf{A}$ , the matrix square root of the covariance,  $\Sigma$ , is required, which can be done via a Cholesky decomposition. This results in a lower triangular matrix,  $\Gamma$ , such that the  $\Sigma = \Gamma \Gamma^T$ . Finally, this can be used to compute

$$\mathbf{A} = \sqrt{n + \gamma} \Gamma. \quad (18)$$

Here,  $n$  is the number of state variables and  $\gamma = \sigma^2(n + \kappa) - n$ , where  $\sigma$  and  $\kappa$  are tuning parameters that control the spread of sigma points around the mean. Typically,  $\sigma \ll 1$ , and  $\kappa = 1$ . Once the sigma points are computed, they are individually passed through either the nonlinear dynamics model (time update) or measurement model (measurement update). Finally, a weighted regression is used to fit a Gaussian distribution to the transformed sigma points, generating an updated mean and covariance.

### 3. Exploiting Triangular Structure

One disadvantage of the UKF is the increased computational load when processing each sigma point. This is especially true when dealing with complex measurement models or numerical integration of the equations of motion. In an effort to reduce the load, a re-ordering of the state variables can allow for a recycling of computed values between sigma points. This form of the UKF is known as the Exploiting Triangular Structure (ETS) UKF [36].

When calculating the sigma points, the matrix square root of the covariance results in a lower triangular matrix,  $\mathbf{\Gamma}$ . Therefore, when forming sigma point  $\chi_i = \mu + \mathbf{A}_i$ ,  $\mathbf{A}_i$  (the  $i$ -th column of  $\mathbf{A}$ ) will be zero in the first  $i - 1$  entries. This means that the first  $i - 1$  entries of  $\chi_i$  will be identical to those entries in the state mean,  $\mu$ . This result can be exploited by rearranging the state to put the state variables that require the most computational load first. For later sigma points that have identical values to the mean, calculations can be reused, saving overall computation time.

During the filter time update, orbit propagation via numerical integration is the most computationally expensive process. Therefore, the parameters required for orbit propagation ( $\mathbf{r}$ ,  $\mathbf{v}$ ,  $\mathbf{a}_e$ ) for each spacecraft should be placed first. Since all other parameters are treated as constants during the time update, their propagation is trivial, meaning they can be placed at the end of the state. The resulting order for state parameters is given by

$$\mathbf{x}_T = [\mathbf{r}^c \quad \mathbf{v}^c \quad \mathbf{a}_e^c \quad \mathbf{r}^d \quad \mathbf{v}^d \quad \mathbf{a}_e^d \quad \text{cdt}^c \quad \mathbf{N}^c \quad \text{cdt}^d \quad \mathbf{N}^{dc} \quad \Delta\mathbf{I}^{dc}]. \quad (19)$$

This order reduces the number of required orbit propagations from 274 to 56 by only requiring 19 sigma points to have a unique orbit state.

The measurement update requires knowledge of the receiver positions,  $\mathbf{r}$ , clock offsets,  $\text{cdt}$ , carrier-phase biases,  $\mathbf{N}$ , and differential ionospheric delay correction,  $\Delta\mathbf{I}$ . Therefore, these parameters should be prioritized, resulting in

$$\mathbf{x}_M = [\mathbf{r}^c \quad \text{cdt}^c \quad \mathbf{r}^d \quad \text{cdt}^d \quad \mathbf{N}^c \quad \mathbf{N}^{dc} \quad \Delta\mathbf{I}^{dc} \quad \mathbf{v}^c \quad \mathbf{a}_e^c \quad \mathbf{v}^d \quad \mathbf{a}_e^d]. \quad (20)$$

With this configuration, the unbiased pseudorange

$$\rho(t) = \|\mathbf{r}(t) - \mathbf{r}(t - \tau)_{GNSS}\| + c(\delta t - \delta t_{GNSS}), \quad (21)$$

which is present in both measurement types, only needs to be calculated a limited number of times for the early sigma points with unique values of  $\mathbf{r}$  and  $\text{cdt}$ . The mean value can then be reused to account for variations in  $\mathbf{N}$  and  $\Delta\mathbf{I}$ , which are added linearly.

The re-ordering is done with a standard permutation matrix,  $\mathcal{P}$ . Being a similarity transform, both the mean and covariance can be rearranged by

$$\mathbf{x}_{(\cdot)} = \mathcal{P}_{(\cdot)}\mathbf{x} \quad (22)$$

$$\mathbf{\Sigma}_{(\cdot)} = \mathcal{P}_{(\cdot)}\mathbf{\Sigma}\mathcal{P}_{(\cdot)}^T, \quad (23)$$

where  $(\cdot)$  represents the transformation for either the time update ( $T$ ) or measurement update ( $M$ ). It should be noted that this permutation retains the positive definiteness of the covariance matrix, which is required for the Cholesky decomposition, as well as for the filter in general.

To demonstrate that the UKF alone is not sufficient to solve the separation-dependent effects, the *Validation* section presents the system without the inclusion of ionospheric model augmentation. It is shown that here are very similar behaviors between the UKF and the EKF when no other modifications are made, resulting in the need for the ionospheric correction as discussed above.

### 4. Hybrid Filter

The idea of saving computational effort can be brought even further by acknowledging that the time update for DiGiTaL happens independently for each spacecraft. The inertial absolute position and velocity for each spacecraft are included in the state, and the absolute orbit is propagated through numerical integration of equations of the motion. This means that the relative state (and therefore the separation) is not needed during this process. The original formulation of DiGiTaL used the EKF to propagate

the absolute orbits with a satisfactory level of accuracy, a process that is unaffected by an increased inter-spacecraft separation. Therefore, a hybrid filter approach can be used.

For the UKF, both the time and measurement updates require an estimate's mean and covariance. The same is true for the EKF, meaning that these functions can be used interchangeably depending on the system. By combining the time update of the EKF with the measurement update of the UKF, the hybrid E/UKF reduces the unnecessary computational load during orbit propagation while still providing better handling of the nonlinearities in the measurements. The hybrid filter design is presented in detail in Algorithm 1. The filter takes as input the previous state mean,  $\mu_{t-1}$ , covariance,  $\Sigma_{t-1}$ , control input,  $\mathbf{u}_{t-1}$ , and sensor measurements,  $\mathbf{y}_t$ . The process noise,  $\mathbf{Q}$ , and measurement noise,  $\mathbf{R}$  are required as well.

---

**Algorithm 1** Extended/Unscented Kalman Filter Algorithm

---

1:	<b>E/UKF</b> ( $\mu_{t-1}, \Sigma_{t-1}, \mathbf{u}_{t-1}, \mathbf{y}_t, \mathbf{Q}, \mathbf{R}$ )	
2:	<b>EKF Time Update</b>	
3:	$\mu_{t t-1} = \mathbf{g}(\mu_{t-1}, \mathbf{u}_{t-1})$	▷ Dynamics model to update mean
4:	$\Sigma_{t t-1} = \Phi \Sigma_{t-1} \Phi^T + \mathbf{Q}$	▷ Update covariance with STM, $\Phi$
5:	<b>UKF Measurement Update</b>	
6:	$\chi_{t t-1} = [\mu_{t t-1} \quad \mu_{t t-1} + \mathbf{A}_{t t-1} \quad \mu_{t t-1} - \mathbf{A}_{t t-1}]$	▷ Form sigma points
7:	$\hat{\mathbf{Y}} = \mathbf{h}(\chi_{t t-1})$	▷ Measurement model
8:	$\hat{\mathbf{y}} = \hat{\mathbf{Y}} \mathbf{w}_m$	▷ Mean measurement
9:	$\Sigma_{yy} = \sum_{i=0}^{2n} w_{c,i} (\hat{\mathbf{Y}}_i - \hat{\mathbf{y}}) (\hat{\mathbf{Y}}_i - \hat{\mathbf{y}})^T + \mathbf{R}$	▷ Measurement covariance
10:	$\Sigma_{xy} = \sum_{i=0}^{2n} w_{c,i} (\chi_{t t-1,i} - \mu_{t t-1}) (\hat{\mathbf{Y}}_i - \hat{\mathbf{y}})^T$	▷ Cross covariance
11:	$\mathbf{K} = \Sigma_{xx} \Sigma_{yy}^{-1}$	▷ Kalman gain
12:	$\mu_{t t} = \mu_{t t-1} + \mathbf{K} (\mathbf{y}_t - \hat{\mathbf{y}})$	▷ Update mean
13:	$\Sigma_{t t} = \Sigma_{t t-1} - \mathbf{K} \Sigma_{yy} \mathbf{K}^T$	▷ Update covariance
14:	<b>Return</b> ( $\mu_{t t}, \Sigma_{t t}$ )	

---

The filter uses the nonlinear dynamics model,  $\mathbf{g}$ , and measurement model  $\mathbf{h}$ , to update the state. For the UKF measurement update, the distribution of sigma point outputs from  $\mathbf{h}$  are weighted together to form an aggregate output. These weights are given by

$$\mathbf{w}_{m,j} = \begin{cases} \frac{\gamma}{n + \gamma}, & \text{for } j = 0 \\ \frac{1}{2(n + \gamma)}, & \text{for } j = 1, \dots, 2n \end{cases} \quad (24)$$

$$\mathbf{w}_{c,j} = \begin{cases} \frac{\gamma}{n + \gamma} + (1 - \sigma^2 + \beta), & \text{for } j = 0 \\ \frac{1}{2(n + \gamma)}, & \text{for } j = 1, \dots, 2n \end{cases} \quad (25)$$

Table 2 shows the execution time for each stage of the filter when run on a Dell XPS 15 Intel Core i7. As expected, the time update in the ETS-UKF is considerably larger than for the EKF. However, the measurement update of the ETS-UKF actually takes less time than the EKF. This is due to the extreme care that is taken during the formulation of the UKF to reuse as many computations as possible, whereas this is not deemed necessary for the EKF. The E/UKF, on the other hand, is able to take the benefits from each type of filter, while removing the cumbersome stages that slow them down. The overall reduction in time between the EKF and the E/UKF also provides confidence that the new DiGiTaL algorithms can run in real time, since the original EKF was already demonstrated in a real-time experiment on flight hardware.

**Table 2:** Execution time for filter variants

Update	EKF [ms]	ETS-UKF [ms]	E/UKF [ms]
Time Update	28.35	257.99	28.51
Measurement Update	1171.7	210.11	210.74
Total Time	1200.05	468.10	239.25

## IV. VALIDATION

To validate these algorithms, testing is performed in the Stanford GNSS and Radiofrequency Testbed for Autonomous Navigation of DSS (GRAND), shown in Figure 3. This environment is designed to enable testing of GNSS-based navigation systems in both a hardware-in-the-loop (HIL) setting for testing GNSS antenna/receiver systems, ISLs, and flight computers, and a software-in-the-loop (SIL) setting for testing algorithms and data flow. To demonstrate the novel DiGiTaL algorithms in a SIL environment, a high-fidelity orbit propagator numerically integrates the orbital and attitude equations of motion to generate ground-truth trajectories. This ground-truth is input into a GNSS Receiver Emulator, which mimics the behavior of the NovAtel OEM628 receiver [26] in DiGiTaL by outputting raw measurements and navigation solutions with representative noise and errors. Uncertainty is included through errors in the GNSS broadcast ephemeris data and atmospheric path delays, as well as sensor noise. The receiver output is then provided to the DiGiTaL software for processing. The flight software is developed in C/C++ and incorporated into the simulation environment through Simulink s-functions, enabling rapid prototyping followed by a seamless transition to a flight computer.

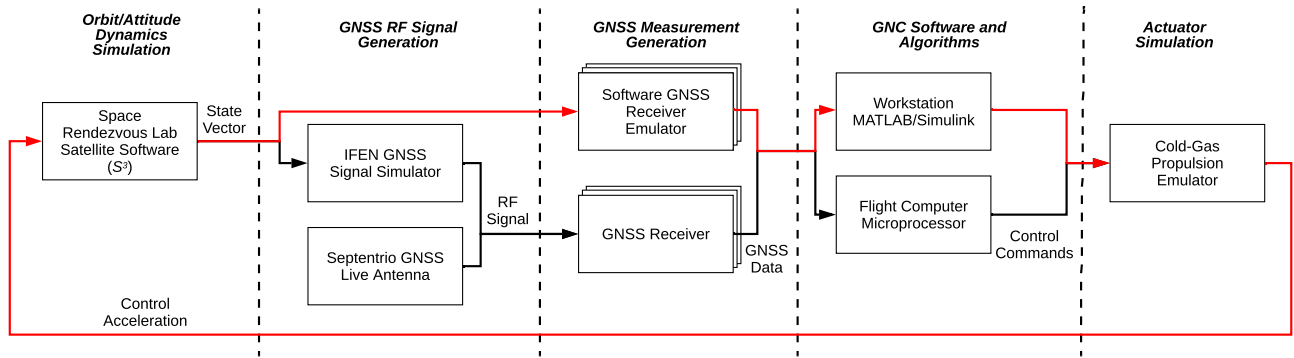


**Figure 3:** GRAND testbed configuration. Red line indicates data flow adopted for testing in this paper [24]

Following the description of the test scenario are a series of results demonstrating different varieties of the DiGiTaL system. This is meant to provide context and justification for each of the augmentations discussed in the *Large-Baseline Estimation* section above. For the purpose of consistency, unless otherwise specified, the test scenario presented in the following section is used as described.

### 1. Test Scenario

A large-baseline scenario representative of the inter-spacecraft separation of the mDOT mission is used to demonstrate the work presented in this paper. The formation will fly in a LEO sun-synchronous orbit with a nominal separation of 500km. The primary goal of this demonstration is to achieve less than 2cm (3D RMS) of relative positioning accuracy. In addition, a comparative assessment is shown using the various formulations presented in order to justify the final design of the navigation filter.

The ground truth orbit simulates the two spacecraft (defined in Table 3 as Occulter and Telescope) under a high-fidelity force model, including the forces listed in Table 4. The NovAtel GNSS Receiver Emulator adds uncertainty into the system through noisy and biased measurements. Gaussian white noise is added to the raw code and phase measurements with standard deviations of 20cm and 1mm, respectively. Precise GNSS constellation data from the International GNSS Service (IGS) is used for measurement generation, while archival broadcast ephemeris data is provided as output from the receiver [37]. Atmospheric effects through ionospheric path delays are added to each signal using the Klobuchar model, with coefficients  $\alpha$  and  $\beta$  provided from IGS and given in Table 5. As previously noted, while this model is also used during the estimation process, the coefficients in the filter are not considered known. Additional random noise is added to the ionospheric delay with a standard deviation of 50% of the nominal value from the Klobuchar model.

**Table 3:** Spacecraft parameters used in ground truth simulation [4]

Parameter	Occluder	Telescope
Mass	250 kg	12 kg
Effective drag area	4 m <sup>2</sup>	0.06 m <sup>2</sup>
Coefficient of drag	2	2
Effective SRP area	4 m <sup>2</sup>	0.06 m <sup>2</sup>
Coefficient of reflectivity	1.8	1.8

**Table 4:** Force models used in ground truth simulation [24]

Force	Model
Gravity field	GGM01S (120x120) [18]
Atmospheric drag	Harris-Preister [33] Cannonball spacecraft model [33]
Solar radiation pressure	Flat plate model [33] Conical Earth shadow model [33]
Geomagnetic and solar flux data	NOA daily KP AP indices
Third-body perturbation	Analytical Sun and Moon [33] DE340 (all planets) [38]
Relativistic corrections	First-order corrections for special and general relativistic effects [33]

**Table 5:** Klobuchar coefficients used in ground truth simulation

Parameter	( $\cdot$ ) <sub>0</sub>	( $\cdot$ ) <sub>1</sub>	( $\cdot$ ) <sub>2</sub>	( $\cdot$ ) <sub>3</sub>
$\alpha$	$0.2142 \times 10^{-7}$	$0.7451 \times 10^{-8}$	$-0.1192 \times 10^{-6}$	0.0
$\beta$	$0.1229 \times 10^6$	0.0	$-0.2621 \times 10^6$	$0.1966 \times 10^6$

A 12-hour experiment takes place, beginning on March 1, 2018 00:00:00.0 UTC. The initial absolute and relative mean orbital elements of the formation are given in Table 6.

**Table 6:** Initial mean orbital elements

Absolute Orbital Elements	Occluder	Relative Orbital Elements	Telescope
Semi-Major Axis ( $a$ ) [km]	6969.28	Relative Semi-Major Axis ( $a\delta a$ ) [m]	1.47
Eccentricity ( $e$ ) [-]	0.00258	Relative Mean Longitude ( $a\delta\lambda$ ) [m]	-500,000
Inclination ( $i$ ) [°]	97.99	Relative Eccentricity ( $a\delta e_x$ ) [m]	-0.36
Longitude of the Ascending Node ( $\Omega$ ) [°]	25.85	Relative Eccentricity ( $a\delta e_y$ ) [m]	300.36
Argument of Perigee ( $\omega$ ) [°]	252.38	Relative Inclination ( $a\delta i_x$ ) [m]	-0.11
Mean Anomaly ( $M$ ) [°]	330.52	Relative Inclination ( $a\delta i_y$ ) [m]	599.32

The resulting relative motion in the Radial-Tangential (RT) and Radial-Normal (RN) planes is shown in Figure 4. Here, it is shown that the separation between the spacecraft is approximately 500km for the duration of the experiment.

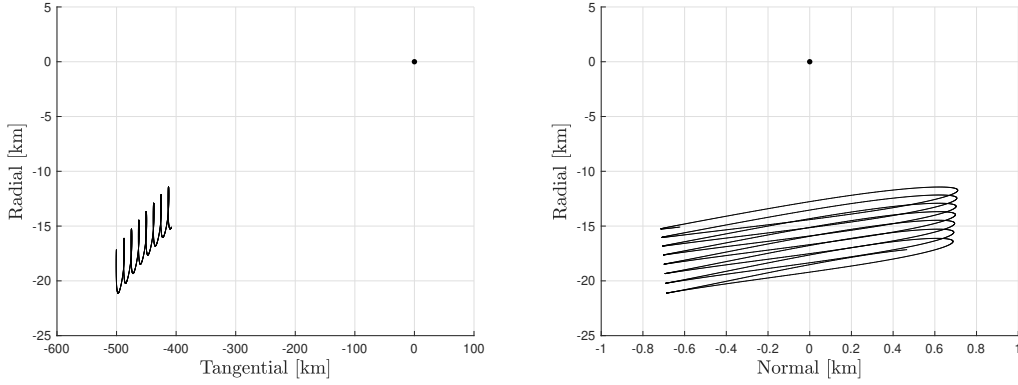


**Figure 4:** Planar relative motion in the RT-plane (left) and RN-plane (right)

The a-priori tuning parameters for the E/UKF are given in Table 7.

**Table 7:** A-priori settings of the E/UKF

Parameter	Value	Parameter	Value
<i>A-priori standard deviation</i>		<i>Process noise</i>	
$\sigma_r$ [m]	100	$\sigma_r$ [mm]	3
$\sigma_v$ [m/s]	0.1	$\sigma_v$ [mm/s]	0.001
$\sigma_{a_R}$ [nm/s <sup>2</sup> ]	1000	$\sigma_{a_R}$ [nm/s <sup>2</sup> ]	1000
$\sigma_{a_T}$ [nm/s <sup>2</sup> ]	2000	$\sigma_{a_T}$ [nm/s <sup>2</sup> ]	1000
$\sigma_{a_N}$ [nm/s <sup>2</sup> ]	750	$\sigma_{a_N}$ [nm/s <sup>2</sup> ]	500
$\sigma_{cdt}$ [m]	100	$\sigma_{cdt}$ [m]	5
$\sigma_N$ [cycles]	100	$\sigma_N$ [cycles]	1
$\sigma_{\Delta I}$ [m]	5	$\sigma_{\Delta I}$ [mm]	10
<i>Auto-correlation time scale</i>		<i>Measurement noise</i>	
$\tau_a$ [s]	900	$\sigma_{pr}$ [m]	0.2
$\tau_{cdt}$ [s]	60	$\sigma_{cp}$ [m]	0.005

## 2. Results

The following presents navigation results from the multiple variations of the DiGiTaL filter described in the *Large-Baseline Estimation* section, providing justification for the final design.

### *Original DiGiTaL Implementation at 2km*

To give a baseline understanding of the results of DiGiTaL, the original implementation is demonstrated at a nominal separation of 2km. The only change to the presented test scenario is that the relative mean longitude ( $a\delta\lambda$ ) is now 2km. Figure 5 shows the relative position and velocity estimates for this experiment. Formal covariance bounds ( $3\sigma$ ) are plotted, in addition to error statistics that are calculated directly from the data. Note that the statistics are calculated once the filter has reached steady state. As shown, there is less than 1cm of relative positioning error, and 0.05mm/s of relative velocity error, which is consistent with previous demonstrations of DiGiTaL [21, 22].

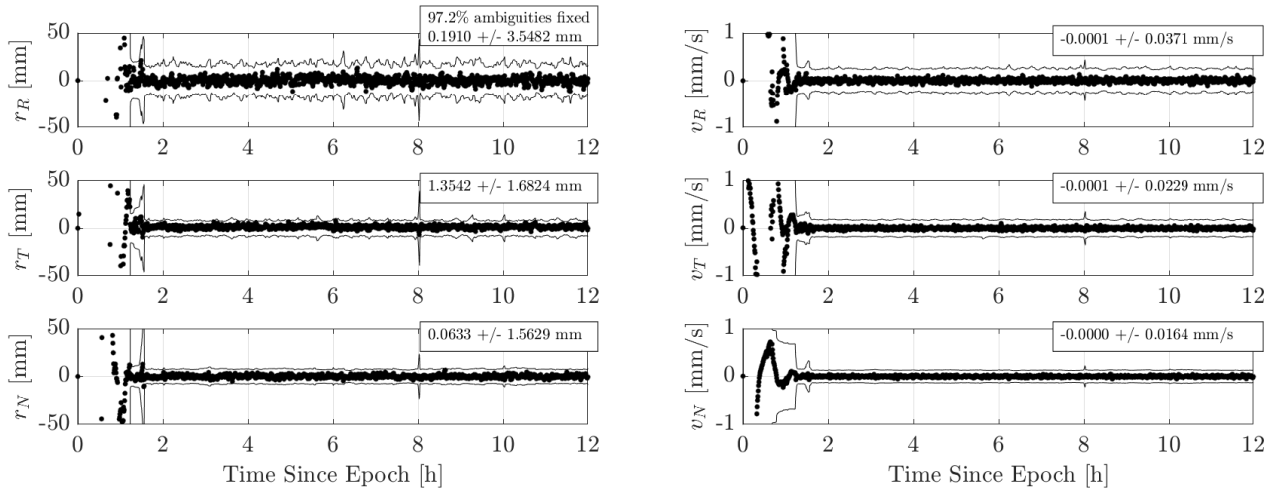


**Figure 5:** Relative position (left) and velocity (right) error for the EKF at 2km separation

### Original DiGiTaL Implementation at 500km

When the original implementation is applied at 500km separation, the performance degrades. Figure 6 shows a bias of 35cm in the tangential position estimate, as well as a 10cm bias in the radial direction. It is particularly detrimental to the filter since the error is completely outside the covariance bounds, indicating that the filter is overconfident and does not know that this bias exists. In addition, the carrier-phase ambiguities were not able to be fixed due to the increased uncertainty, resulting in larger standard deviations in both position and velocity errors.

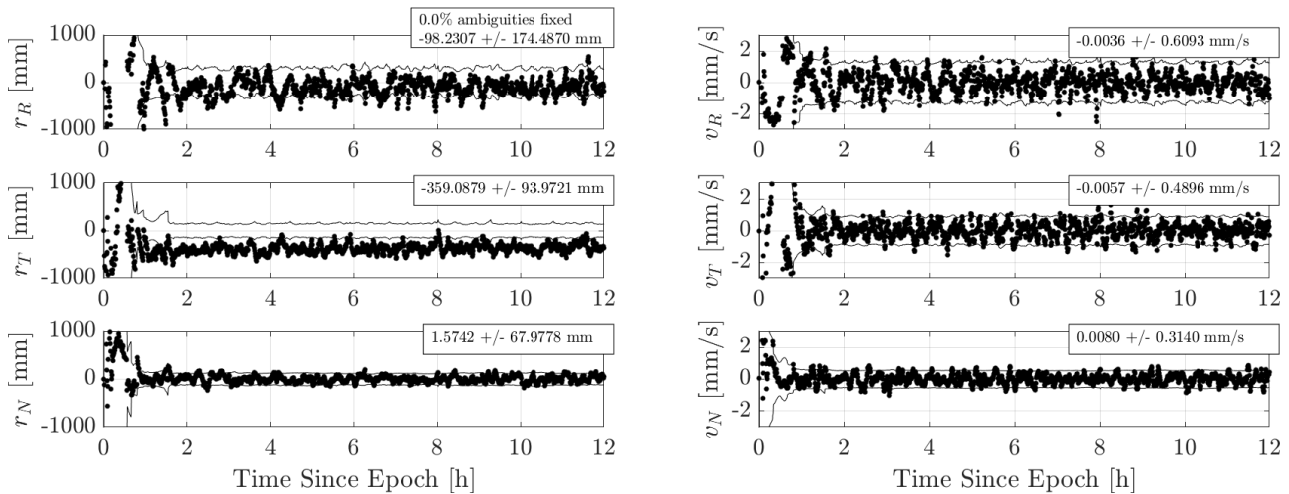


**Figure 6:** Relative position (left) and velocity (right) error for the EKF at 500km separation

### Ionospheric Delay Augmentation

Applying the ionospheric path delay augmentation to the original filter, the navigation solution does not improve. The 35cm bias that was seen in the filter without ionospheric estimation has been reduced to 15cm. However, the spread of the error has increased, particularly in the radial direction. While there is perhaps a better tuning of the filter to reduce the large variations in the estimate, the tangential bias still too large to meet the required accuracy. Additionally, the uncertainty in the system did not allow for successful IAR, except in 0.2% of candidate ambiguities.

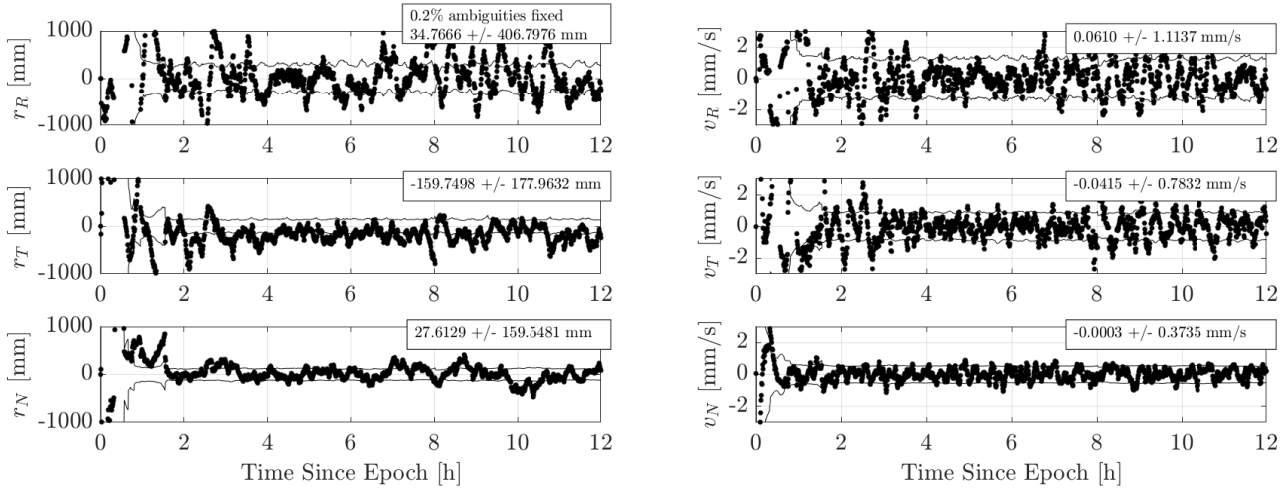


**Figure 7:** Relative position (left) and velocity (right) error for the EKF with ionospheric correction at 500km separation

### Unscented Kalman Filter

When the EKF is switched to the ETS-UKF without the ionospheric path delay augmentation, we see similar results as to the original implementation. In particular, a bias is seen in the tangential position of more than 35cm.

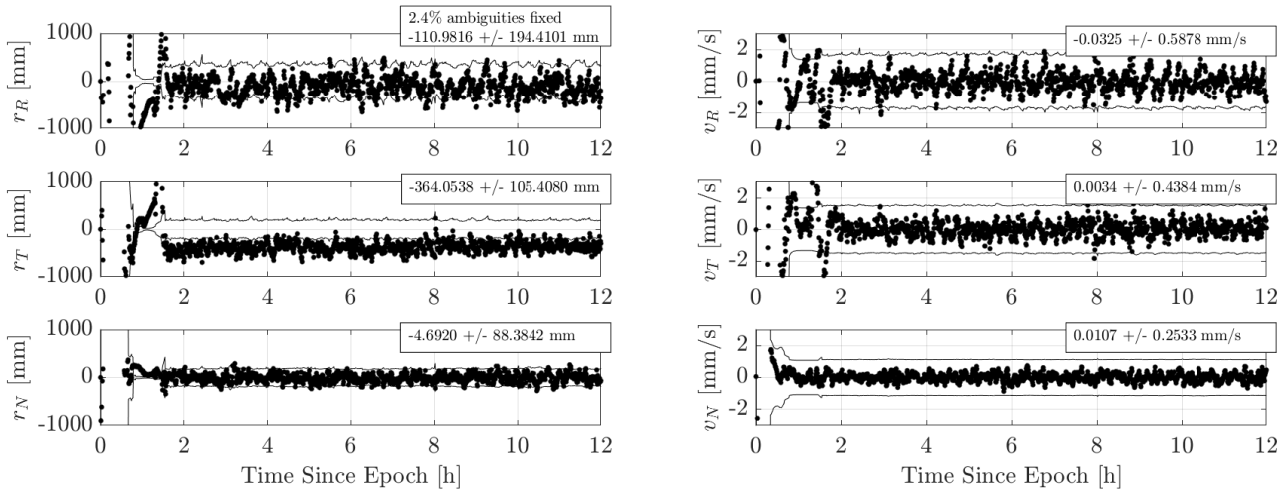


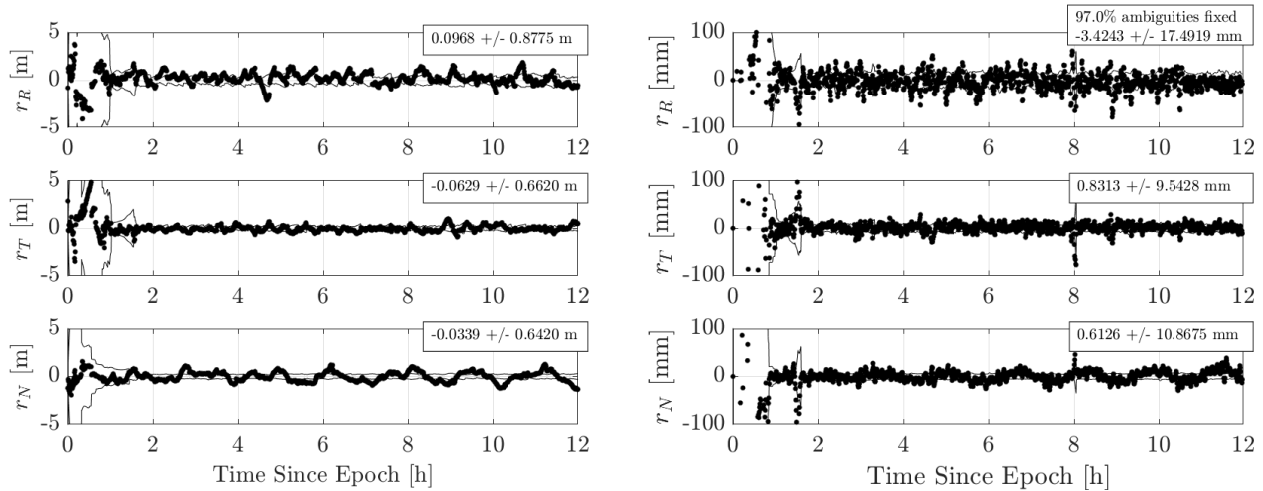
**Figure 8:** Relative position (left) and velocity (right) error for the ETS-UKF at 500km separation

For completeness, it should be reiterated that the hybrid E/UKF alone performs nearly identically to the ETS-UKF implementation with the exception of the computational savings. Therefore, the results are not presented.

### Extended/Unscented Filter with Ionospheric Delay Augmentation

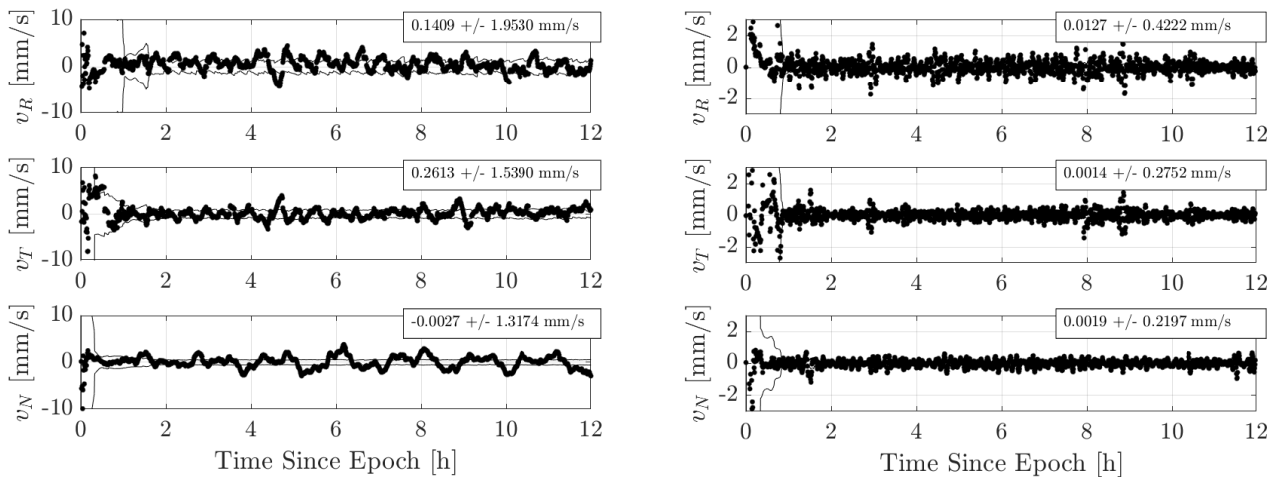
The following takes each of the previous augmentations and combines them to enable precision navigation at large separations. Expanded results are shown for this case. Figure 9 shows the absolute and relative positioning estimate error from the E/UKF. Prior to the one-hour mark, IAR is activated and there is a sudden decrease in both the spread of the error and the covariance bounds. This is because the filter now treats the carrier-phase biases as deterministic after fixing, removing a source of uncertainty. After IAR initialization, 97% of the eligible ambiguities are fixed due to the strict validity checks and data editing. During steady-state, the absolute error is 1m (3D, RMS), while the relative error is 2cm (3D, RMS), achieving the desired level of accuracy and meeting the requirements for mDOT. It should be noted, however, that this experiment does not include the

frequent maneuvers that will occur during the science phase of the mDOT mission.



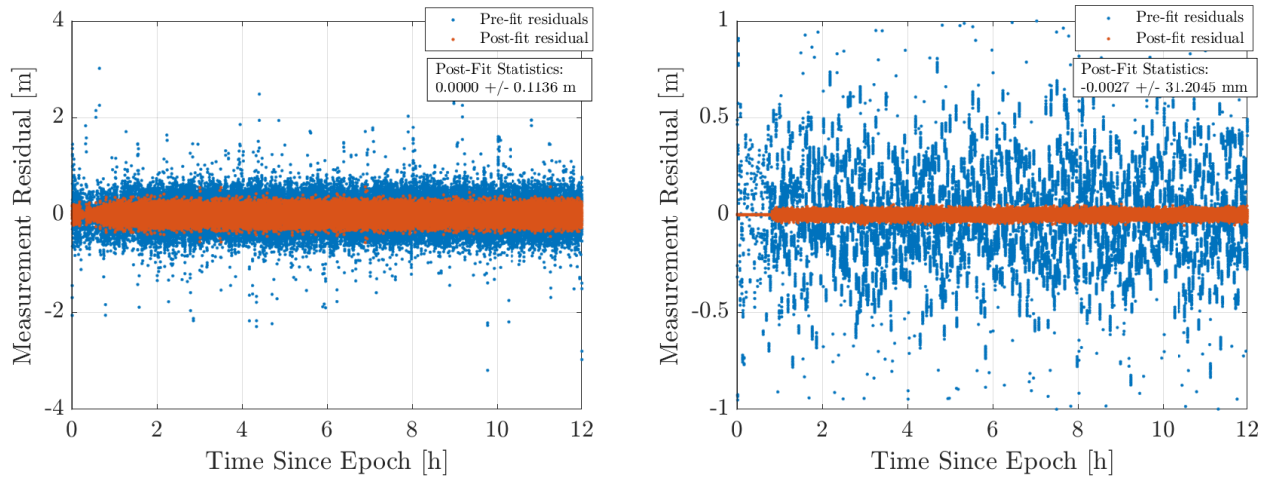
**Figure 9:** E/UKF absolute (left) and relative (right) position estimate error

In a similar fashion, the absolute and relative velocity estimate errors are shown in Figure 10. The trends in the error and covariance are the same as for the positioning estimates, with a sudden decrease after IAR activation. Here, the absolute and relative errors are 2.7mm/s and 0.5mm/s (3D, RMS), respectively.



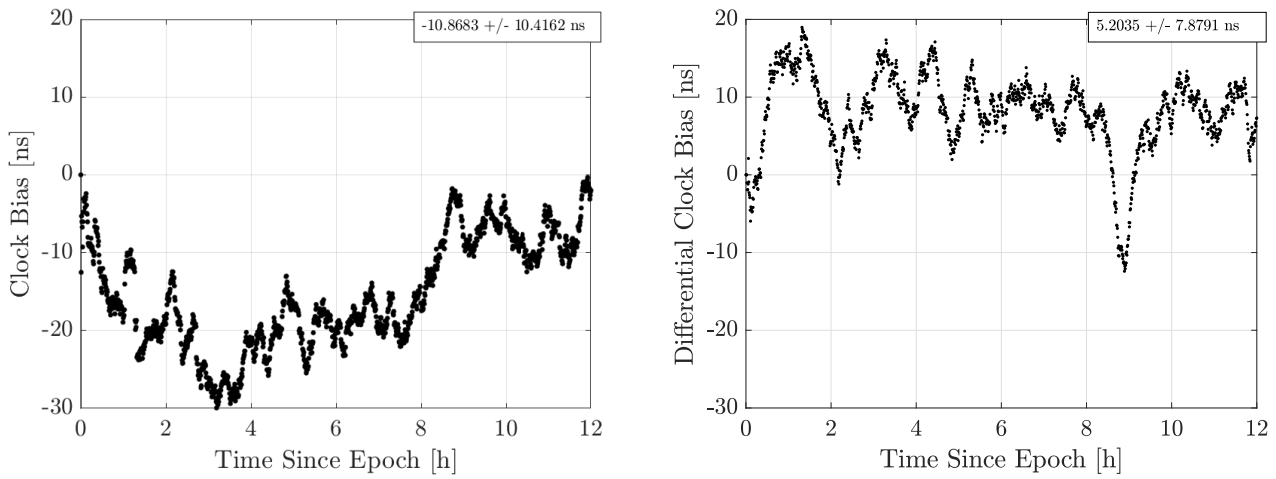
**Figure 10:** E/UKF absolute (left) and relative (right) velocity estimate error

The measurement residuals for each type are shown in Figure 11. It is important to note the sudden increase in post-fit residuals after the activation of IAR, particularly in the SDCP measurements. Prior to this, the carrier-phase bias acts as a free parameter on each measurement that the filter can adjust to minimize the residual. Once that free parameter is lost, the filter behavior becomes more consistent with the expected noise of the system, indicating a healthy filter.



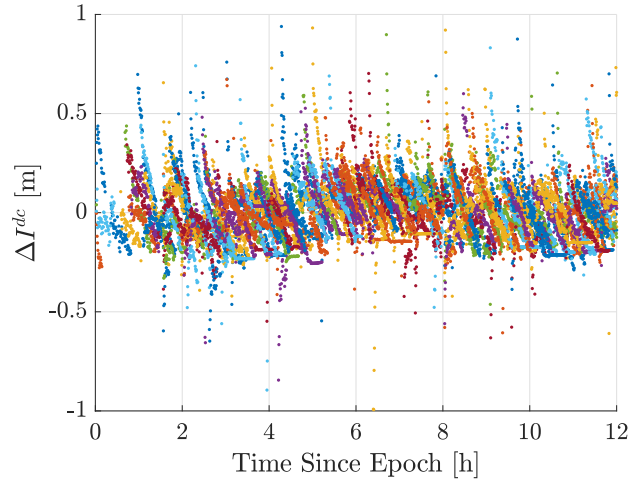
**Figure 11:** Measurement residuals for the GRAPHIC (left) and SDCP (right) data types, including pre-fit (blue) and post-fit (orange)

Figure 12 shows the absolute and relative clock bias between each receiver. Note that the differential clock bias can be used as a metric for synchronicity between the spacecraft. Since both of the clocks are steered towards GPS system time, the resulting estimated synchronicity is less than 10 nanoseconds.



**Figure 12:** Absolute (left) and relative (right) receiver clock bias

Finally, Figure 13 shows the estimated ionospheric path delay correction term over each tracking arc. The general trend is that the estimated correction decreases over the arc on a given channel, correcting for up to 1m of differential ionospheric delay on each channel.



**Figure 13:** Estimated differential ionospheric delay correction

## V. CONCLUSIONS

This work presents a novel navigation methodology to extend the capabilities of on-board GNSS-based relative orbit determination to inter-spacecraft separations up to 500km. In particular, this methodology is applied to the Distributed Multi-GNSS Timing and Localization system, a plug-and-play navigation payload for nanosatellite swarms capable to providing centimeter-level relative positioning accuracy in real time.

To account for the large differential ionospheric path delays at the increased separation, the single-difference carrier-phase measurement model is augmented with a new term that combines the Klobuchar model with a differential correction that is included in the estimation state. In addition, the measurement update of the filter now uses the unscented Kalman filter update, creating a hybrid extended/unscented filter. This E/UKF allows for the better handling of nonlinearities in the measurements while limiting the computational cost of state propagation. To further reduce computational effort, the measurement update uses the Exploiting Triangular Structure UKF, where the state is permuted to maximize the number of reused calculations. This structural change led to decreased computation time when compared to both the traditional EKF and UKF, indicating that the E/UKF can perform in real time.

The new algorithms were demonstrated in a software-in-the-loop experiment, where a high-fidelity orbit propagator simulated two spacecraft representative of the Miniaturized Distributed Occulter/Telescope mission with a nominal separation of 500km. A GNSS receiver emulator used the ground truth information to generate realistic measurements, including atmospheric effects, broadcast ephemeris errors, and measurement noise. The GNSS data was provided to the flight software, where the orbit determination algorithms demonstrated relative positioning error of 2cm (3D, RMS) and relative velocity errors of 0.5mm/s (3D, RMS). This gives confidence that these algorithms can meet the needs to future missions such as mDOT.

Further testing and evaluation of these algorithms is planned. In particular, hardware-in-the-loop verification will ensure flight readiness of DiGiTaL for mDOT, VISORS, and DWARF by enabling precision navigation at variable baselines in real time. To increase the fidelity of the mission scenarios, realistic maneuvers will be added in a closed-loop simulation to verify that these algorithms maintain a high level of precision in the presence of maneuver execution uncertainty. In addition to flight opportunities, these algorithms can be applied beyond binary formations to arbitrarily sized swarms with large inter-spacecraft separations, allowing for a variety of advanced mission concepts.

## ACKNOWLEDGEMENTS

The authors would like to thank the King Abdulaziz City for Science and Technology (KACST), and the NASA Small Spacecraft Technology Program for funding the DiGiTaL project through grant number NNX16AT31A.

## REFERENCES

- [1] J. Kolmas, P. Banazadeh, A. W. Koenig, B. Macintosh, and S. D’Amico, “System design of a miniaturized distributed occulter/telescope for direct imaging of star vicinity,” in *2016 IEEE Aerospace Conference*, Big Sky, Montana, March 5–12, 2016, pp. 1–11.

- [2] B. Sullivan, D. Barnhart, L. Hill, P. Oppenheimer, B. L. Benedict, G. Van Ommering, L. Chappell, J. Ratti, and P. Will, "DARPA phoenix payload orbital delivery system (PODs): "FedEx to GEO"," in *AIAA SPACE 2013 Conference and Exposition*, San Diego, California, September 10–13, 2013, pp. 1–14.
- [3] O. Montenbruck, G. Allende-Alba, J. Rosello, M. Tossaint, and F. Zangerl, "Precise orbit and baseline determination for the SAOCOM-CS bistatic radar mission," *Navigation: Journal of The Institute of Navigation*, vol. 65, no. 1, pp. 15–24, 2018.
- [4] S. D'Amico, A. Koenig, B. Macintosh, and D. Mauro, "System design of the miniaturized distributed occulter/telescope (mDOT) science mission," in *33rd Annual Conference on Small Satellites*, Logan, Utah, August 3–8, 2019, pp. 1–20.
- [5] A. Koenig, S. D'Amico, and E. G. Lightsey, "Formation flying orbit and control concept for the VISORS mission," in *AIAA Scitech 2021 Forum*, January 11–15 & 19–21, 2021.
- [6] S. E. Palo, M. Pilinski, J. P. Thayer, W. Q. Lohmeyer, K. M. Lemmer, S. D'Amico, E. G. Lightsey, and S. Latif, "The space weather atmospheric reconfigurable multiscale experiment (SWARM-EX): A new nsf supported cubesat project," in *American Geophysical Union Fall Meeting 2020*, December 1–17, 2020.
- [7] A. Koenig, "Formation design of distributed telescopes in earth orbit with application to high-contrast imaging," Ph.D. dissertation, Stanford University, Stanford, California, 2019.
- [8] S. D'Amico, "Collaborative research: Cubesat ideas lab: Virtual super-resolution optics with reconfigurable swarms (VISORS)," NSF Award Database, 2019, [https://www.nsf.gov/awardsearch/showAward?AWD\\_ID=1936542&HistoricalAwards=false](https://www.nsf.gov/awardsearch/showAward?AWD_ID=1936542&HistoricalAwards=false).
- [9] S. D'Amico and R. Carpenter, "Satellite formation flying and rendezvous," in *Global Positioning System: Theory and Applications*, B. Parkinson and J. Spilker, Eds., 2018, ch. 50.
- [10] J.-S. Ardaens, S. D'Amico, and O. Montenbruck, "Final commissioning of the PRISMA GPS navigation system," in *22nd International Symposium on Spaceflight Dynamics*, San Jose dos Campos, Brazil, February 28–March 4, 2011, pp. 1–16.
- [11] S. D'Amico, "Autonomous formation flying in low earth orbit," Ph.D. dissertation, Delft University of Technology, Delft, Netherlands, 2010.
- [12] S. D'Amico, J. Ardaens, and R. Larsson, "Spaceborne autonomous formation-flying experiment on the PRISMA mission," *Journal of Guidance, Control, and Dynamics*, vol. 35, no. 3, pp. 834–850, 2012.
- [13] S. D'Amico, J. Ardaens, S. De Florio, O. Montenbruck, S. Persson, and R. Noteborn, "GPS-based spaceborne autonomous formation flying experiment (SAFE) on PRISMA: initial commissioning," in *AIAA/AAS Astrodynamics Specialist Conference*, Toronto, Canada, August 2–5, 2010, pp. 1–15.
- [14] N. Roth, "Navigation and control design for the CanX-4/-5 satellite formation flying mission," Ph.D. dissertation, University of Toronto, Toronto, Canada, 2010.
- [15] G. Bonin, N. Roth, S. Armitage, J. Newman, B. Risi, and R. E. Zee, "CanX-4 and CanX-5 precision formation flight: Mission accomplished!" in *29th AIAA/USU Conference on Small Satellites*, August 8–13, 2015, pp. 1–15.
- [16] N. Roth, B. Risi, C. Grant, and R. Zee, "Flight results from the CanX-4 and CanX-5 formation flying mission," in *Proceedings of the Small Satellites, Systems & Services Symposium (4S)*, Valletta, Malta, May 30–June 3, 2016, pp. 1–15.
- [17] R. Kroes, "Precise relative positioning of formation flying spacecraft using GPS." Ph.D. dissertation, Delft University of Technology, Delft, Netherlands, 2006.
- [18] B. D. Tapley, S. Bettadpur, M. Watkins, and C. Reigber, "The gravity recovery and climate experiment: Mission overview and early results," *Geophysical Research Letters*, vol. 31, no. 9, 2004.
- [19] W. Bertiger, Y. Bar-Sever, S. Bettadpur, C. Dunn, B. Haines, G. Kruizinga, D. Kuang, S. Nandi, L. Romans, M. Watkins *et al.*, "GRACE: millimeters and microns in orbit," in *Institute of Navigation GPS*, Portland, Oregon, September 24–27, 2002.
- [20] S. D'Amico, R. Hunter, and C. Baker, "Distributed timing and localization (DiGiTaL)," ARC-EDAA-TN45564, 2017, [https://damicos.people.stanford.edu/sites/g/files/sbiybj2226/f/digital\\_factsheet\\_2019.pdf](https://damicos.people.stanford.edu/sites/g/files/sbiybj2226/f/digital_factsheet_2019.pdf).
- [21] V. Giraldo and S. D'Amico, "Distributed multi-GNSS timing and localization for nanosatellites," *Navigation*, vol. 66, no. 4, pp. 729–746, 2019.
- [22] V. Giraldo, M. Chernick, and S. D'Amico, "Guidance, navigation, and control for the DWARF formation-flying mission," in *AAS/AIAA Astrodynamics Specialist Conference*, South Lake Tahoe, California, August 9–13, 2020, pp. 1–19.

- [23] J. A. Klobuchar, "Ionospheric time-delay algorithm for single-frequency gps users," *IEEE Transactions on aerospace and electronic systems*, no. 3, pp. 325–331, 1987.
- [24] V. Giraldo and S. D'Amico, "Development of the Stanford GNSS navigation testbed for distributed space systems," in *Institute of Navigation, International Technical Meeting*, Reston, Virginia, January 29–February 1, 2018, pp. 837–856.
- [25] Tallysman, *A Tallysman Acutenna TW3972E High Gain Embedded Triple Band GNSS Antenna + L-band Correction Services*, 2016, TW3972E.
- [26] NovAtel, *OEM 628 High Performance GNSS Receiver*, 2016, D15588.
- [27] P. Misra and P. Enge, "Global positioning system: signals, measurements and performance second edition," *Global Positioning System: Signals, Measurements And Performance Second Editions*, 2006.
- [28] T. P. Yunck, "Coping with the atmosphere and ionosphere in precise satellite and ground positioning," *Geophysical Monograph Series*, vol. 73, pp. 1–16, 1993.
- [29] P. Barneveld, O. Montenbruck, and P. Visser, "Differential ionospheric effects in gps based navigation of formation flying spacecraft," in *3rd International Symposium on Formation Flying, Missions and Technology*, Noordwijk, Netherlands, April 23–25, 2008, pp. 1–16.
- [30] X. W. Chang, X. Yang, and T. Zhou, "Mlambda: a modified lambda method for integer least-squares estimation," *Journal of Geodesy*, vol. 79, no. 9, pp. 552–565, 2005.
- [31] S. Verhagen, "The gnss integer ambiguities: Estimation and validation," Ph.D. dissertation, Delft University of Technology, Delft, Netherlands, 2004.
- [32] S. Verhagen, "Integer ambiguity validation: An open problem?" *GPS Solutions*, vol. 8, no. 1, pp. 36–43, 2004.
- [33] O. Montenbruck and E. Gill, *Satellite Orbits*. Springer, 2000, vol. 2.
- [34] J. Sullivan and S. D'Amico, "Nonlinear kalman filtering for improved angles-only navigation using relative orbital elements," *Journal of Guidance, Control, and Dynamics*, vol. 40, no. 9, pp. 2183–2200, 2017.
- [35] N. Stacy and S. D'Amico, "Adaptive and dynamically constrained process noise estimation for orbit determination," in *AAS/AIAA Astrodynamics Specialist Conference*, Portland, Maine, August 11–15, 2019, pp. 1–25.
- [36] N. Stacey and S. D'Amico, "Autonomous swarming for simultaneous navigation and asteroid characterization," in *AAS/AIAA Astrodynamics Specialist Conference*, 2018.
- [37] J. M. Dow, R. E. Neilan, and C. Rizos, "The international gnss service in a changing landscape of global navigation satellite systems," *Journal of geodesy*, vol. 83, no. 3-4, pp. 191–198, 2009.
- [38] W. M. Folkner, J. G. Williams, D. H. Boggs, R. S. Park, and P. Kuchynka, "The planetary and lunar ephemerides de430 and de431," *Interplanetary Network Progress Report*, vol. 196, no. 1, 2014.